

Crystal-field effects in the formation of Wigner-molecule supercrystals in moiré TMD superlattices

Constantine Yannouleas* and Uzi Landman†

School of Physics, Georgia Institute of Technology, Atlanta, Georgia 30332-0430

(Dated: 27 May 2024)

For moiré bilayer TMD superlattices, full-configuration-interaction (FCI) calculations are presented that take into account both the intra-moiré-quantum-dot (MQD) charge-carrier Coulombic interactions, as well as the crystal-field effect from the surrounding moiré pockets (inter-moiré-QD interactions). Such FCI calculations enable an effective computational embedding strategy and allow for a complete interpretation of the counterintuitive experimental observations reported recently in the context of moiré TMD superlattices at integer fillings $\nu = 2$ and 4. Two novel states of matter are reported: (i) a genuinely quantum-mechanical supercrystal of *sliding* Wigner molecules (WMs) for unstrained moiré TMD materials (when the crystal field is commensurate with the trilobal symmetry of the confining potential in each embedded MQD) and (ii) a supercrystal of *pinned* Wigner molecules when strain is involved and the crystal field is incommensurate with the trilobal symmetry of the confining potential in each embedded MQD. The case of $\nu = 3$ is an exception, in that both unstrained and strained cases produce a supercrystal of pinned WMs, which is due to the congruence of intrinsic (that of the WM) and external (that of the confining potential of the MQD) C_3 point-group symmetries. Furthermore, it is shown that the unrestricted Hartree-Fock approach fails to describe the supercrystal of sliding WMs in the unstrained case, providing a qualitative agreement only in the case of a supercrystal of pinned WMs.

I. INTRODUCTION

Earlier studies have revealed a novel fundamental-physics aspect in artificial twodimensional (2D) nanosystems in the regime of strong interelectronic correlations, namely formation of quantum Wigner molecules (WMs), originally described theoretically [1–26] in 2D semiconductor (parabolic, elliptic, and double-well) quantum dots (QDs), as well as in trapped ultracold atoms, and subsequently observed experimentally in GaAs QDs [27–30], Si/SiGe QDs [31], planar germanium QDs [32] and 1D carbon-nanotubes [33].

Remarkably, most recent work [34–36] has extended the WM portfolio to the newly emerging and highly regarded (due to the potential for fundamental-physics discoveries and for advancing quantum-device applications) field of transition-metal dichalcogenide (TMD) moiré materials and superlattices. Specifically, TMD moiré superlattices are highly pursued for solving the question of scalability in quantum computer architectures.

Building on the demonstrated formation [34] of WMs in the isolated moiré pockets [most often referred to as moiré quantum dots (MQDs)] at integer fillings, we investigate here the effects arising from embedding such single MQDs in the moiré superlattice structure, which is the actual system that was addressed experimentally [36]. Specifically, this paper addresses the key question whether the experimental observations in the unstrained-lattice case do reflect formation of a collective WM supercrystal, i.e., a novel, more complex insulating phase of matter beyond the well-known generalized Wigner crystal, or the

trivial case of a collection of independent MQDs. The present investigations (see below) support formation of a WM supercrystal [37] having sliding WMs as building blocks for $\nu = 2$ or $\nu = 4$, with the filling $\nu = 3$ being an exception having a pinned WM as a building block.

Specifically, this paper focuses on the effects on WM formation in a given MQD resulting from the crystal-field generated by the charge carriers (of same nature) in the surrounding MQDs (moiré pockets) located at the apices of a regular hexagon in the TMD moiré superlattice. This approach is inspired by the well-known crystal-field theory [38, 39] in molecular physics, and is applicable here because the moiré lattice constant a_M is much larger than the extent of the Wigner molecule within a single MQD. Two different computational methodologies will be used in this endeavor, namely: (i) the full configuration interaction (FCI) [8, 9, 14, 17, 21, 22, 26, 40–45] and (ii) the spin-and-space unrestricted Hartree-Fock (sS-UHF) [1, 5, 14, 46, 47].

II. MANY-BODY HAMILTONIAN (INCLUDING CRYSTAL FIELD FROM SURROUNDING MOIRÉ POCKETS)

Following earlier established literature [34, 36, 48–50], we approximate the potential of the 2D TMD moiré superlattice that confines the extra charge carriers as

$$V(\mathbf{r}) = -2v_0 \sum_{i=1}^3 \cos(\mathbf{G}_i \cdot \mathbf{r} + \phi), \quad (1)$$

where $\mathbf{G}_i = [(4\pi/\sqrt{3}a_M)(\sin(2\pi i/3), \cos(2\pi i/3))]$ are the moiré reciprocal lattice vectors. The materials specific parameters of $V(\mathbf{r})$ are v_0 (which can also be experimen-

* Constantine.Yannouleas@physics.gatech.edu

† Uzi.Landman@physics.gatech.edu

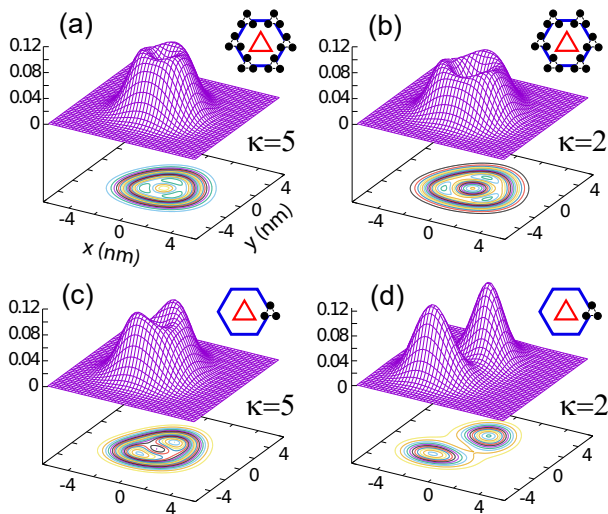


FIG. 1. FCI ground-state (with total spin $S = 0$) charge densities for $N = 2$ holes in the embedded central MQD (red triangle in the schematics) taking into consideration the crystal-field effect generated by the charge carriers in the surrounding six moiré pockets (see blue hexagon, with radius a_M , in the schematics). (a) and (c) $\kappa = 5$ in agreement with the case of a TMD moiré superlattice in hBN environment. (b) and (d) were calculated, for purpose of comparison, with $\kappa = 2$, corresponding to a stronger Coulomb repulsion. In (a) and (b), all six surrounding MQDs (see schematics) were populated with $Q = Ne$ charge carriers. In (c) and (d), only one of the surrounding MQDs (the one to the right, see schematics) has been populated with $Q = Ne$ charge carriers. The charge-carrier distributions in each surrounding MQD have been represented by three point charges $Q/3$ placed at the apices of an equilateral triangle (see schematics), with radius $a_M/6$. Remaining parameters: effective mass $m^* = 0.90m_e$, moiré lattice constant $a_M = 9.8$ nm, depth of a moiré pocket $v_0 = 10.3$ eV, and $\phi = 20^\circ$. Charge densities are in units of $1/\text{nm}^2$.

tally controlled through voltage biasing), the moiré lattice constant a_M , and the angle ϕ . a_M is typically of the order of 10 nm, which is much larger than the lattice constant of the monolayer TMD material (typically a few Å).

The parameter ϕ controls the strength of the trilobal C_3 anisotropy in each MQD potential pocket. This trilobal anisotropy can be seen by expanding $V(\mathbf{r})$ in Eq. (1) in powers of r , and defining an approximate confining potential, $V_{\text{MQD}}(\mathbf{r})$, for a single MQD as follows:

$$V_{\text{MQD}}(\mathbf{r}) \equiv V(\mathbf{r}) + 6v_0 \cos(\phi) \approx m^* \omega_0^2 r^2 / 2 + \mathcal{C} \sin(3\theta) r^3. \quad (2)$$

with $m^* \omega_0^2 = 16\pi^2 v_0 \cos(\phi) / a_M^2$, and $\mathcal{C} = 16\pi^3 v_0 \sin(\phi) / (3\sqrt{3} a_M^3)$; m^* is the effective mass and the expansion of $V(\mathbf{r})$ can be restricted to the terms up to r^3 . (r, θ) are the polar coordinates of the position vector \mathbf{r} .

The effective many-body Hamiltonian associated with a given MQD embedded in the moiré superlattice is given

by

$$H_{\text{MB}} = H_{\text{MQD}} + H_{\text{CF}}, \quad (3)$$

where

$$H_{\text{MQD}} = \sum_{i=1}^N \left\{ \frac{\mathbf{p}_i^2}{2m^*} + V_{\text{MQD}}(\mathbf{r}_i) \right\} + \sum_{i < j}^N \frac{e^2}{\kappa |\mathbf{r}_i - \mathbf{r}_j|}, \quad (4)$$

with κ being the dielectric constant, and

$$H_{\text{CF}} = \sum_{i=1}^N \sum_{j=1}^{3\mathcal{M}} \frac{eQ}{3\kappa |\mathbf{r}_i - \mathbf{R}_j|} \quad (5)$$

is the crystal-field potential from the surrounding moiré pockets, \mathcal{M} denoting the number of surrounding moiré pockets populated with charge carriers, and the \mathbf{R}_j 's being the positions of the point charges that mimic the charge carrier distributions. In each one of the surrounding moiré pockets, we use three point charges at the apices of an equilateral triangle with a total charge $Q = Ne$, thus respecting the C_3 trilobal symmetry; see solid dots in the schematics in the figures.

A brief outline of the FCI and sS-UHF methodologies, used to solve the corresponding many-body Schrödinger equation, is presented in the Appendices. Before proceeding with the computational results, we point out that the arrangement having the equilateral three-point-charge distributions in all the six surrounding moiré pockets [see schematic in Fig. 1(a)] displays an overall C_6 point-group symmetry, which is commensurate with the trilobal C_3 symmetry associated with the potential confinement [Eq. (2)] of a single MQD. Below, we will investigate the effect of both such a commensurate crystal field, as well as the effect of an incommensurate crystal field (IcCF) generated by placing the three-point-charge distribution in only one of the six surrounding moiré pockets [see schematic in Fig. 1(c)].

III. RESULTS FOR FILLING FACTOR $\nu = 2$

The FCI and sS-UHF charge densities (CDs) for a moiré TMD (e.g., WS_2 [36]) superlattice at integer filling factor $\nu = 2$ calculated using the many-body Hamiltonian (...) are displayed in Fig. 1 and Fig. 2, respectively. The configuration of the equilateral three-point-charge distributions that mimic the crystal-field effect from the surrounding six moiré pockets is illustrated in the schematics drawn in the upper right corner of each frame; see figure captions for details and parameters. The total charge associated with each equilateral three-point-charge distribution is $Q = 2e$. (Note that Q/e can be taken different than ν in the case of a noninteger filling.)

The FCI calculations [see Figs. 1(a) and 1(b)] demonstrate that the full crystal-field effect (all six surrounding moiré pockets are contributing) maintains the charge densities that are associated with sliding WMs. Namely,

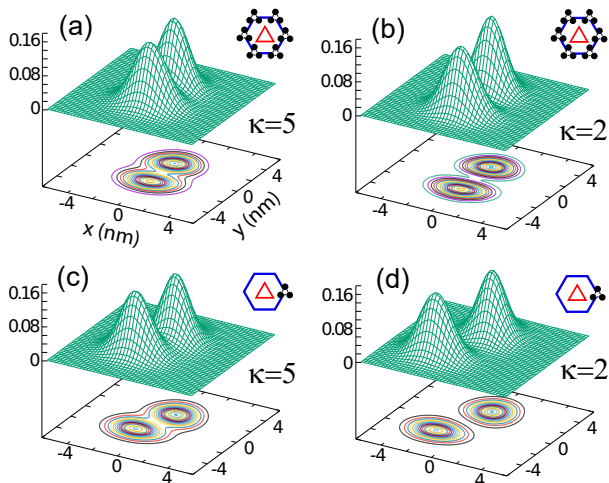


FIG. 2. sS-UHF ground-state (with total-spin projection $S_z = 0$) charge densities for $N = 2$ holes in the central MQD (red triangle in the schematics) taking into consideration the crystal-field effect generated by the charge carriers in the surrounding six moiré pockets (see blue hexagon, with radius a_M , in the schematics). (a) and (c) $\kappa = 5$ in agreement with the case of a TMD moiré superlattice in hBN environment. (b) and (d) were calculated, for purpose of comparison, with $\kappa = 2$, corresponding to a stronger Coulomb repulsion. In (a) and (b), all six surrounding MQDs (see schematics) were populated with $Q = Ne$ charge carriers. In (c) and (d), only one of the surrounding MQDs (the one to the right, see schematics) has been populated with $Q = Ne$ charge carriers. The charge-carrier distributions in each surrounding MQD have been represented by three point charges $Q/3$ placed at the apices of an equilateral triangle (see schematics), with radius $a_M/6$. Remaining parameters: effective mass $m^* = 0.90m_e$, moiré lattice constant $a_M = 9.8$ nm, depth of a moiré pocket $v_0 = 10.3$ eV, and $\phi = 20^\circ$. Charge densities are in units of $1/\text{nm}^2$.

the CDs preserve the C_3 symmetry of the confining single-moiré-pocket potential, as was the case with the isolated MQDs [34]. Note that even a stronger Coulomb repulsion ($\kappa = 2$ instead of $\kappa = 5$, which corresponds to the experimental setup) does not destroy the the C_3 symmetry; see Fig. 1(b). This symmetry-preserving behavior is counterintuitive for a crystalline material in that the CDs necessarily exhibit three modest humps instead of the naive expectation of a symmetry-breaking double hump associated with two Wigner-crystal-type [51–54] localized charge carriers (one hump per charge carrier). Note further that this counterintuitive behavior is in remarkable agreement with the recent experimental findings [36] for the unstrained case at filling $\nu = 2$.

The CDs in Figs. 2(a) and 2(b) demonstrate that the sS-UHF is unable to properly describe the unstrained TMD moiré supercrystal at filling $\nu = 2$. Indeed, these sS-UHF CDs exhibit a pinned WM with two well-localized humps in accordance with the traditional Wigner-crystal-type [51–54] expectation (one hump per charge carrier). We stress again that these sS-UHF CDs

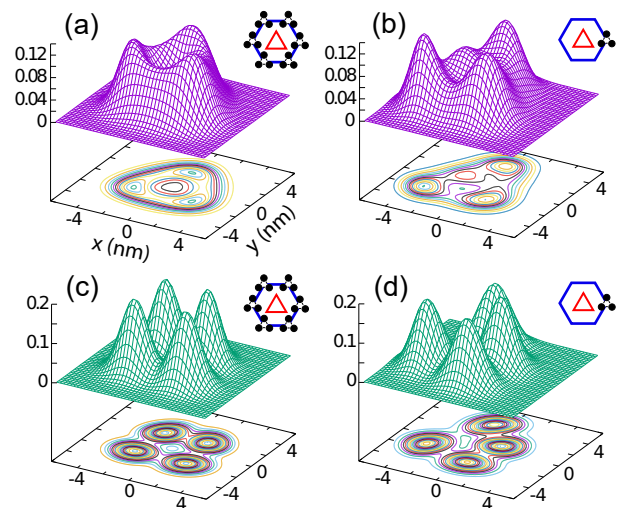


FIG. 3. Charge densities for $N = 4$ holes in the central MQD (red triangle in the schematics) taking into consideration the crystal-field effect generated by the charge carriers in the surrounding six moiré pockets (see blue hexagon, with radius a_M , in the schematics). (a) and (b) FCI ground-states (with total spin $S = 1$ and total-spin projection $S_z = 0$). (c) and (d) sS-UHF ground-states (with total spin projection $S_z = 0$). Dielectric constant $\kappa = 5$ in agreement with the case of a TMD moiré superlattice in an hBN environment. In (a) and (c), all six surrounding MQDs (see schematics) were populated with $Q = Ne$ charge carriers. In (b) and (d), only one of the surrounding MQDs (the one to the right, see schematics) has been populated with $Q = Ne$ charge carriers. The charge-carrier distributions in each surrounding MQD have been represented by three point charges $Q/3$ placed at the apices of an equilateral triangle (see schematics), with radius $a_M/6$. Remaining parameters: effective mass $m^* = 0.90m_e$, moiré lattice constant $a_M = 9.8$ nm, depth of a moiré pocket $v_0 = 10.3$ eV, and $\phi = 20^\circ$. Charge densities are in units of $1/\text{nm}^2$.

do break the C_3 symmetry of the single-moiré-pocket confinement and disagree with the experimental observations [36].

Heretofore, we used a crystal field with C_6 symmetry (associated with that of the six surrounding moiré pockets), which is commensurate with the C_3 symmetry of the confinement of the embedded MQD. A natural question arising at this point concerns the effect of a crystal field that has a symmetry non-commensurate with the C_3 symmetry of the single MQD. Experimentally, such a non-commensurability was generated [36] by deforming the moiré lattice through straining. Here, we generate a non-commensurability situation by maintaining the equilateral three-point-charge configuration only in a single moiré pocket [the one on the right; see schematics in Figs. 1(c,d) and 2(c,d)].

From the FCI CDs in Figs. 1(c,d), it is apparent that the IcCF produces an azimuthally *pinned* WM exhibiting two antipodal humps. These pinned-WM CDs do break the C_3 symmetry of the single MQD. In addition,

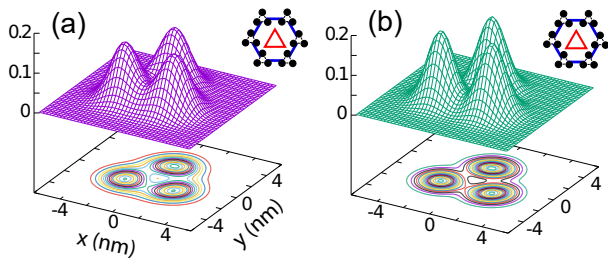


FIG. 4. Charge densities for $N = 3$ holes in the central MQD (red triangle in the schematics) taking into consideration the crystal-field effect generated by the charge carriers in the surrounding six moiré pockets (see blue hexagon, with radius a_M , in the schematics). (a) FCI ground-states (with total spin $S = 1/2$ and total-spin projection $S_z = 1/2$). (b) sS-UHF ground-states (with total spin projection $S_z = 1/2$). Dielectric constant $\kappa = 5$ in agreement with the case of a TMD moiré superlattice in an hBN environment. In (a) and (b), all six surrounding MQDs (see schematics) were populated with $Q = Ne$ charge carriers. The charge-carrier distributions in each surrounding MQD have been represented by three point charges $Q/3$ placed at the apices of an equilateral triangle (see schematics), with radius $a_M/6$. Remaining parameters: effective mass $m^* = 0.90m_e$, moiré lattice constant $a_M = 9.8$ nm, depth of a moiré pocket $v_0 = 10.3$ eV, and $\phi = 20^\circ$. Charge densities are in units of $1/\text{nm}^2$.

the extent of localization for each charge carrier becomes more pronounced for stronger Coulomb repulsion; compare the case of $\kappa = 5$ [Fig. 1(c)] to $\kappa = 2$ [Fig. 1(d)]. Concerning the corresponding sS-UHF CDs, it is obvious that, in qualitative agreement with the FCI result, the IcCF CDs result also in pinned two-humped WMs, exhibiting, nevertheless, a stronger charge-carrier localization; contrast Fig. 1(c) to Fig. 2(c) and Fig. 1(d) to Fig. 2(d). We mention here that our IcCF FCI CDs are in agreement with the recent experimental observations [36] of two-humped pinned WMs per moiré pocket in the case of *strained* moiré superlattices at a filling $\nu = 2$.

IV. RESULTS FOR FILLING FACTOR $\nu = 4$

The ability of the crystal-field with the commensurate C_6 symmetry to preserve, and even enhance, the formation of a quantum sliding WM in the central MQD is revealed in an even more spectacular way in the case of the filling factor $\nu = 4$, where Ref. [36] has reported within each MQD the observation of CDs with 3 humps (C_3 symmetry) for the unstrained lattice, but with 4 humps (broken symmetry) for the strained lattice. Our FCI CDs that take into account the crystal-field effect are in agreement with the experiment; see the 3-hump, sliding-WM CD in Fig. 3(a) (commensurate crystal field) and the 4-hump, distorted-pinned-WM CD in Fig. 3(b) (IcCF). We further note that the sS-UHF fails to describe the sliding WM, yielding instead a broken- C_3 -symmetry CD (pinned WM) with 4 well defined humps even for the case of the

commensurate crystal field; see Fig. 3(c). In the case of an IcCF, the sS-UHF agrees qualitatively with the FCI CD as it describes a deformed, 4-hump, pinned WM; compare Fig. 3(b) and Fig. 3(d), the charge-carrier localization being more pronounced in the sS-UHF CD.

V. RESULTS FOR FILLING FACTOR $\nu = 3$

Compared to the cases of $\nu = 2$ and $\nu = 4$, the case of $\nu = 3$ is exceptional, a fact that was reported already in Ref. [34] where formation of WMs was investigated for the case of an isolated MQD in the absence of a crystal field from the surrounding moiré pockets. Specifically, the 3-hump pinned WM in the central MQD has a C_3 symmetry which coincides with that of the confining potential. This congruence of intrinsic and external point-group symmetries prohibits the formation of a sliding WM and yields a strongly pinned WM. The commensurate crystal field does not alter this CD distribution, a fact that is reflected in the FCI calculation [see Fig. 4(a)]. In the $\nu = 3$ case, the sS-UHF result is in qualitative agreement with the FCI one [see Fig. 4(b)], with the charge-carrier localization, however, being more pronounced in the sS-UHF case. Again, it is remarkable that our FCI results (including the crystal-field effect) for $\nu = 3$ are in excellent agreement with the experiment [36].

VI. SUMMARY

Taking into consideration (via a computational embedding scheme) both the intra-moiré-QD charge-carrier interactions in the embedded MQD, as well as the crystal-field effect from the surrounding moiré pockets (inter-moiré-QD interactions), and using the full-configuration-interaction methodology, we offered a complete interpretation of the counterintuitive experimental observations reported in Ref. [36] in the context of moiré TMD superlattices at integer fillings $\nu = 2$ and 4. In particular, our results demonstrate that these experimental observations reflect the interplay between two novel states of matter; namely, (i) a supercrystal of sliding Wigner molecules [55] for unstrained moiré TMD materials (when the crystal field is commensurate with the trilobal symmetry of the confining potential in each MQD) and (ii) a supercrystal of pinned Wigner molecules when strain is involved and the crystal field is non-commensurate with the trilobal symmetry of the confining potential in each MQD. The case of $\nu = 3$ is an exception, in that both unstrained and strained cases produce a supercrystal of pinned WMs; this is due to the congruence of intrinsic (that of the WM) and external (that of the confining potential of the MQD) C_3 point-group symmetries.

Furthermore, we demonstrated that the UHF approach (invoked in Refs. [36, 56]) utterly fails to describe the genuinely quantum-mechanical supercrystal of sliding WMs

in the unstrained case, providing a qualitative agreement only in the case of a supercrystal of pinned WMs.

The insights gained in this work through systematic comparisons, employing the UHF method with exact diagonalization (FCI) calculations as benchmarks, provide impetus and pathways for the development of effective strategies for advancing economically feasible and accurate computational methodologies for treating strongly-correlated many-body states in materials, including the electron (hole) Wigner-molecular TMD superlattice systems studied here.

VII. ACKNOWLEDGEMENTS

This work has been supported by a grant from the Air Force Office of Scientific Research (AFOSR) under Award No. FA9550-21-1-0198. Calculations were carried out at the GATECH Center for Computational Materials Science.

Appendix A: THE CONFIGURATION INTERACTION METHOD

The full configuration interaction (FCI) methodology has a long history, starting in quantum chemistry; see Refs. [40, 45]. The method was adapted to two dimensional problems and found extensive applications in the fields of semiconductor quantum dots [8, 9, 14, 16, 26, 42–44] and of the fractional quantum Hall effect [10, 22].

Our 2D FCI is described in our earlier publications. The reader will find a comprehensive exposition in Appendix B of Ref. [26], where the method was applied to GaAs double-quantum-dot quantum computer qubits. We specify that, in the application to moiré DQDs, we keep similar space orbitals, $\varphi_j(x, y)$, $j = 1, 2, \dots, K$, that are employed in the building of the single-particle basis of spin-orbitals used to construct the Slater determinants Ψ_I , which span the many-body Hilbert space [see Eq. (B4) in Ref. [26]; the index I counts the Slater determinants]. The orbitals $\varphi_j(x, y)$ are determined as solutions (in Cartesian coordinates) of the auxiliary Hamiltonian

$$H_{\text{aux}} = \frac{\mathbf{p}^2}{2m^*} + \frac{1}{2}m^*\omega_0^2(x^2 + y^2), \quad (\text{A1})$$

where $m^*\omega_0^2 = 16\pi^2v_0 \cos(\phi)/a_M^2$, i.e., only the isotropic parabolic (harmonic) contribution of the MQD confinement $V_{\text{MQD}}(\mathbf{r})$ [see Eqs. (2) and (4) in the main text] is included.

The matrix elements $\langle \varphi_i(x, y) | \sin(3\theta)r^3 | \varphi_j(x, y) \rangle$ of the anisotropic term in the MQD confinement are calculated analytically using the algebraic language MATHEMATICA [57] and the Hermite-to-Laguerre (Cartesian-to-polar) transformations listed in Ref. [58], whereas the matrix elements $\langle \varphi_i(x, y) | H_{\text{CF}} | \varphi_j(x, y) \rangle$ of the crystal field are calculated numerically.

Following Ref. [26], we use a sparse-matrix eigensolver based on Implicitly Restarted Arnoldi methods to diagonalize the many-body Hamiltonian in Eq. (3) of the main text. We stress that the FCI conserves both the total spin and the total-spin projection.

Appendix B: THE SPIN-AND-SPACE UNRESTRICTED HARTREE-FOCK

Early on in the context of 2D materials, the spin-and-space unrestricted Hartree-Fock (sS-UHF) was employed in Ref. [1] to describe formation of Wigner molecules at the mean-field level. This methodology employs the Pople-Nesbet equations [14, 45]. The sS-UHF WMs are self-consistent solutions of the Pople-Nesbet equations that are obtained by relaxing both the total-spin and space symmetry requirements. For a detailed description of the Pople-Nesbet equations in the context of three-dimensional natural atoms and molecules, see Ch. 3.8 in Ref. [45]. For a detailed description of the Pople-Nesbet equations in the context of two-dimensional artificial atoms and semiconductor quantum dots, see Sec. 2.1 of Ref. [14]. We note that the Pople-Nesbet equations conserve the total-spin projection, but not the total spin. Convergence of the self-consistent iterations was achieved in all cases by mixing the input and output charge densities at each iteration step. The convergence criterion was set to a difference of 10^{-12} meV between the input and output total UHF energies at the same iteration step.

Appendix C: CHARGE DENSITIES FROM FCI AND UHF WAVE FUNCTIONS

The FCI single-particle density (charge density) is the expectation value of a one-body operator

$$\rho(\mathbf{r}) = \langle \Phi^{\text{FCI}} | \sum_{i=1}^N \delta(\mathbf{r} - \mathbf{r}_i) | \Phi^{\text{FCI}} \rangle, \quad (\text{C1})$$

where Φ^{FCI} denotes the many-body (multi-determinantal) FCI wave function, namely,

$$\Phi^{\text{FCI}}(\mathbf{r}_1, \dots, \mathbf{r}_N) = \sum_I C_I \Psi_I(\mathbf{r}_1, \dots, \mathbf{r}_N), \quad (\text{C2})$$

with $\Psi_I(\mathbf{r})$ denoting the Slater determinants that span the many-body Hilbert space. The expansion coefficients C_I are a byproduct of the exact diagonalization of the many-body Hamiltonian H_{MB} .

For the sS-UHF case, one substitutes Φ^{FCI} in Eq. (C1) with the single-determinant, $\Psi^{\text{UHF}}(\mathbf{r})$, solution of the Pople-Nesbet equations. $\Psi^{\text{UHF}}(\mathbf{r})$ is built out from the

UHF spin-orbitals whose space part has the form:

$$u_i^\alpha = \sum_{\mu=1}^K C_{\mu i}^\alpha \varphi_\mu, \quad i = 1, \dots, K, \quad (\text{C3})$$

and

$$u_i^\beta = \sum_{\mu=1}^K C_{\mu i}^\beta \varphi_\mu, \quad i = 1, \dots, K, \quad (\text{C4})$$

where the expansion coefficients $C_{\mu i}^\alpha$ and $C_{\mu i}^\beta$ are solutions

of the Pople-Nesbet equations, with α and β denoting up and down spins, respectively.

The UHF expression for the charge density simplifies to:

$$\rho^{\text{UHF}}(\mathbf{r}) = \sum_{i=1}^{N^\alpha} |u_i^\alpha(\mathbf{r})|^2 + \sum_{j=1}^{N^\beta} |u_j^\beta(\mathbf{r})|^2, \quad (\text{C5})$$

with N^α , N^β being the number of lowest-energy occupied spin-up and spin-down orbitals, respectively.

-
- [1] C. Yannouleas and U. Landman, Spontaneous Symmetry Breaking in Single and Molecular Quantum Dots, *Phys. Rev. Lett.* **82**, 5325–5328 (1999).
- [2] R. Egger, W. Häusler, C. H. Mak, and H. Grabert, Crossover from Fermi liquid to Wigner molecule behavior in quantum dots, *Phys. Rev. Lett.* **82**, 3320–3323 (1999).
- [3] C. Yannouleas and U. Landman, Collective and Independent-Particle Motion in Two-Electron Artificial Atoms, *Phys. Rev. Lett.* **85**, 1726–1729 (2000).
- [4] A. V. Filinov, M. Bonitz, and Y. E. Lozovik, Wigner Crystallization in Mesoscopic 2D Electron Systems, *Phys. Rev. Lett.* **86**, 3851–3854 (2001).
- [5] C. Yannouleas and U. Landman, Strongly correlated wavefunctions for artificial atoms and molecules, *Journal of Physics: Condensed Matter* **14**, L591–L598 (2002).
- [6] S. A. Mikhailov, Two ground-state modifications of quantum-dot beryllium, *Phys. Rev. B* **66**, 153313 (2002).
- [7] A. Harju, S. Siljamäki, and R. M. Nieminen, Wigner molecules in quantum dots: A quantum monte carlo study, *Phys. Rev. B* **65**, 075309 (2002).
- [8] C. Yannouleas and U. Landman, Two-dimensional quantum dots in high magnetic fields: Rotating-electron-molecule versus composite-fermion approach, *Phys. Rev. B* **68**, 035326 (2003).
- [9] M. B. Tavernier, E. Anisimovas, F. M. Peeters, B. Szafran, J. Adamowski, and S. Bednarek, Four-electron quantum dot in a magnetic field, *Phys. Rev. B* **68**, 205305 (2003).
- [10] C. Yannouleas and U. Landman, Structural properties of electrons in quantum dots in high magnetic fields: Crystalline character of cusp states and excitation spectra, *Phys. Rev. B* **70**, 235319 (2004).
- [11] B. Szafran, F. M. Peeters, S. Bednarek, and J. Adamowski, Anisotropic quantum dots: Correspondence between quantum and classical Wigner molecules, parity symmetry, and broken-symmetry states, *Phys. Rev. B* **69**, 125344 (2004).
- [12] I. Romanovsky, C. Yannouleas, L. O. Baksmaty, and U. Landman, Bosonic molecules in rotating traps, *Phys. Rev. Lett.* **97**, 090401 (2006).
- [13] Y. Li, C. Yannouleas, and U. Landman, From a few to many electrons in quantum dots under strong magnetic fields: Properties of rotating electron molecules with multiple rings, *Phys. Rev. B* **73**, 075301 (2006).
- [14] C. Yannouleas and U. Landman, Symmetry breaking and quantum correlations in finite systems: Studies of quantum dots and ultracold Bose gases and related nuclear and chemical methods, *Reports on Progress in Physics* **70**, 2067–2148 (2007).
- [15] Z. Dai, J.-L. Zhu, N. Yang, and Y. Wang, Spin-dependent rotating Wigner molecules in quantum dots, *Phys. Rev. B* **76**, 085308 (2007).
- [16] Y. Li, C. Yannouleas, and U. Landman, Three-electron anisotropic quantum dots in variable magnetic fields: Exact results for excitation spectra, spin structures, and entanglement, *Phys. Rev. B* **76**, 245310 (2007).
- [17] L. O. Baksmaty, C. Yannouleas, and U. Landman, Rapidly rotating boson molecules with long- or short-range repulsion: An exact diagonalization study, *Phys. Rev. A* **75**, 023620 (2007).
- [18] A. Ghosal, A. D. Güçlü, C. J. Umrigar, D. Ullmo, and H. U. Baranger, Incipient Wigner localization in circular quantum dots, *Phys. Rev. B* **76**, 085341 (2007).
- [19] N. Yang, J.-L. Zhu, and Z. Dai, Rotating Wigner molecules and spin-related behaviors in quantum rings, *Journal of Physics: Condensed Matter* **20**, 295202 (2008).
- [20] I. Romanovsky, C. Yannouleas, and U. Landman, Edge states in graphene quantum dots: Fractional quantum Hall effect analogies and differences at zero magnetic field, *Phys. Rev. B* **79**, 075311 (2009).
- [21] B. B. Brandt, C. Yannouleas, and U. Landman, Double-well ultracold-fermions computational microscopy: Wave-function anatomy of attractive-pairing and Wigner-molecule entanglement and natural orbitals, *Nano Letters* **15**, 7105–7111 (2015).
- [22] C. Yannouleas and U. Landman, Exact closed-form analytic wave functions in two dimensions: Contact-interacting fermionic spinful ultracold atoms in a rapidly rotating trap, *Phys. Rev. Research* **3**, L032028 (2021).
- [23] H. E. Ercan, S. N. Coppersmith, and M. Friesen, Strong electron-electron interactions in Si/SiGe quantum dots, *Phys. Rev. B* **104**, 235302 (2021).
- [24] J. C. Abadillo-Uriel, B. Martinez, M. Filippone, and Y.-M. Niquet, Two-body Wigner molecularization in asymmetric quantum dot spin qubits, *Phys. Rev. B* **104**, 195305 (2021).
- [25] C. Yannouleas and U. Landman, Wigner molecules and hybrid qubits, *J. Phys.: Condens. Matter (Letter)* **34**, 21LT01 (2022).
- [26] C. Yannouleas and U. Landman, Molecular formations and spectra due to electron correlations in three-electron hybrid double-well qubits, *Phys. Rev. B* **105**, 205302 (2022).

- (2022).
- [27] C. Ellenberger, T. Ihn, C. Yannouleas, U. Landman, K. Ensslin, D. Driscoll, and A. C. Gossard, Excitation Spectrum of Two Correlated Electrons in a Lateral Quantum Dot with Negligible Zeeman Splitting, *Phys. Rev. Lett.* **96**, 126806 (2006).
- [28] S. Kalliakos, M. Rontani, V. Pellegrini, C. P. García, A. Pinczuk, G. Goldoni, E. Molinari, L. N. Pfeiffer, and K. W. West, A molecular state of correlated electrons in a quantum dot, *Nature Physics* **4**, 467–471 (2008).
- [29] W. Jang, M.-K. Cho, H. Jang, J. Kim, J. Park, G. Kim, B. Kang, H. Jung, V. Umansky, and D. Kim, Single-Shot Readout of a Driven Hybrid Qubit in a GaAs Double Quantum Dot, *Nano Letters* **21**, 4999–5005 (2021).
- [30] W. Jang, J. Kim, J. Park, G. Kim, M.-K. Cho, H. Jang, S. Sim, B. Kang, H. Jung, V. Umansky, and D. Kim, Wigner-molecularization-enabled dynamic nuclear polarization, *Nature Communications* **14**, 2948 (2023).
- [31] J. Corrigan, J. P. Dodson, H. E. Ercan, J. C. Abadillo-Uriel, B. Thorgrimsson, T. J. Knapp, N. Holman, T. McJunkin, S. F. Neyens, E. R. MacQuarrie, R. H. Foote, L. F. Edge, M. Friesen, S. N. Coppersmith, and M. A. Eriksson, Coherent control and spectroscopy of a semiconductor quantum dot Wigner molecule, *Phys. Rev. Lett.* **127**, 127701 (2021).
- [32] F. D. Palma, F. Oppliger, W. Jang, S. Bosco, M. Janík, S. Calcaterra, G. Katsaros, G. Isella, D. Loss, and P. Scarlino, Strong hole-photon coupling in planar ge: probing the charge degree and wigner molecule states (2023), [arXiv:2310.20661 \[quant-ph\]](https://arxiv.org/abs/2310.20661).
- [33] S. Pecker, F. Kuemmeth, A. Secchi, M. Rontani, D. C. Ralph, P. L. McEuen, and S. Ilani, Observation and spectroscopy of a two-electron Wigner molecule in an ultraclean carbon nanotube, *Nature Physics* **9**, 576–581 (2013).
- [34] C. Yannouleas and U. Landman, Quantum Wigner molecules in moiré materials, *Phys. Rev. B* **108**, L121411 (2023).
- [35] C. Yannouleas and U. Landman, Wigner-molecule supercrystal in transition metal dichalcogenide moiré superlattices: Lessons from the bottom-up approach, *Phys. Rev. B* **109**, L121302 (2024).
- [36] H. Li, Z. Xiang, A. P. Reddy, T. Devakul, R. Sailus, R. Banerjee, T. Taniguchi, K. Watanabe, S. Tongay, A. Zettl, L. Fu, M. F. Crommie, and F. Wang, Wigner molecular crystals from multi-electron moiré artificial atoms (2023), [arXiv:2312.07607 \[cond-mat.mes-hall\]](https://arxiv.org/abs/2312.07607).
- [37] We note that the experimental results for the unstrained case in Ref. [36] were necessarily interpreted with formation of sliding WMs in *isolated* MQDs (for $N = 2$ confined charge carriers, see Refs. [34, 36]; for $N = 4$ confined charge carriers, see Ref. [34]), given the fact that the mean-field Hartree-Fock approach (that allows calculations for a large number of charge carriers distributed over several moiré pockets) is unreliable [35, 36] for describing sliding WMs.
- [38] H. Bethe, Termaufspaltung in Kristallen, *Annalen der Physik* **395**, 133–208 (1929).
- [39] J. H. Van Vleck, Theory of the variations in paramagnetic anisotropy among different salts of the iron group, *Phys. Rev.* **41**, 208–215 (1932).
- [40] I. Shavitt, The history and evolution of configuration interaction, *Molecular Physics* **94**, 3–17 (1998).
- [41] C. Yannouleas and U. Landman, Electron and boson clusters in confined geometries: Symmetry breaking in quantum dots and harmonic traps, *Proceedings of the National Academy of Sciences* **103**, 10600–10605 (2006).
- [42] M. Rontani, C. Cavazzoni, D. Bellucci, and G. Goldoni, Full configuration interaction approach to the few-electron problem in artificial atoms, *The Journal of Chemical Physics* **124**, 124102 (2006).
- [43] Y. Li, C. Yannouleas, and U. Landman, Artificial quantum-dot Helium molecules: Electronic spectra, spin structures, and Heisenberg clusters, *Phys. Rev. B* **80**, 045326 (2009).
- [44] C. Yannouleas and U. Landman, Valleytronic full configuration-interaction approach: Application to the excitation spectra of si double-dot qubits, *Phys. Rev. B* **106**, 195306 (2022).
- [45] A. Szabo and N. S. Ostlund, *Modern Quantum Chemistry* (McGraw-Hill, New York, 1989) For the Slater-Condon rules, see Chap. 4.
- [46] C. Yannouleas and U. Landman, Magnetic-field manipulation of chemical bonding in artificial molecules, *International Journal of Quantum Chemistry* **90**, 699–708 (2002).
- [47] C. Yannouleas and U. Landman, Formation and control of electron molecules in artificial atoms: Impurity and magnetic-field effects, *Phys. Rev. B* **61**, 15895–15904 (2000).
- [48] F. Wu, T. Lovorn, E. Tutuc, and A. H. MacDonald, Hubbard model physics in transition metal dichalcogenide moiré bands, *Phys. Rev. Lett.* **121**, 026402 (2018).
- [49] M. Angeli and A. H. MacDonald, Γ -valley transition metal dichalcogenide moiré bands, *Proceedings of the National Academy of Sciences* **118**, e2021826118 (2021).
- [50] Y. Zhang, N. F. Q. Yuan, and L. Fu, Moiré quantum chemistry: Charge transfer in transition metal dichalcogenide superlattices, *Phys. Rev. B* **102**, 201115 (2020).
- [51] E. Wigner, On the interaction of electrons in metals, *Phys. Rev.* **46**, 1002–1011 (1934).
- [52] E. Wigner, Effects of the electron interaction on the energy levels of electrons in metals, *Trans. Faraday Soc.* **34**, 678–685 (1938).
- [53] H. Li, S. Li, E. C. Regan, D. Wang, W. Zhao, S. Kahn, K. Yumigeta, M. Blei, T. Taniguchi, K. Watanabe, S. Tongay, A. Zettl, M. F. Crommie, and F. Wang, Imaging two-dimensional generalized Wigner crystals, *Nature* **597**, 650–654 (2021).
- [54] Y.-C. Tsui, M. He, Y. Hu, E. Lake, T. Wang, K. Watanabe, T. Taniguchi, M. P. Zaletel, and A. Yazdani, Direct observation of a magnetic-field-induced wigner crystal, *Nature* **628**, 287–292 (2024).
- [55] When the QD confinement possesses circular symmetry, the sliding WMs were earlier referred to as rotating WMs or rotating electron molecules [8, 14].
- [56] A. P. Reddy, T. Devakul, and L. Fu, Artificial Atoms, Wigner Molecules, and an Emergent Kagome Lattice in Semiconductor Moiré Superlattices, *Phys. Rev. Lett.* **131**, 246501 (2023).
- [57] Wolfram Research, Inc., *Mathematica*, Version 13.2, Champaign, IL, 2022.
- [58] I. Kimel and L. Elias, Relations between Hermite and Laguerre Gaussian modes, *IEEE Journal of Quantum Electronics* **29**, 2562–2567 (1993).